Global Flow Measurement Workshop
22 - 24 October 2024

Technical Paper

Providing confidence in the use of CFD-based correction factors for flare gas flow rates

Lefki Germanou, TÜV SÜD National Engineering Laboratory
David Braybrook, TÜV SÜD National Engineering Laboratory
Sandy Black, TÜV SÜD National Engineering Laboratory

ABSTRACT

This study presents a methodology for validating CFD-derived correction factors (k-factors) for ultrasonic flare gas meters, and calculating their associated errors and uncertainties, a critical step for accurate flare gas measurement. Experimental tests were performed at TÜV SÜD National Engineering Laboratory across various scaled-down flow configurations, while the CFD validation followed the ASME V&V 20-2009 Standard procedures. A suggested methodology is provided for implementing these results in actual flare gas systems, enabling the calculation of calibrated CFD k-factors and their uncertainties, and thus supporting a comprehensive uncertainty budget for flare gas flows. This work contributes to the development of more robust and standardised methodologies for accurate flare gas measurement, enhancing both regulatory compliance and environmental performance.

1 INTRODUCTION

Accurate flare gas measurement is essential for minimizing environmental impact, ensuring regulatory compliance, improving operational efficiency, and contributing to global efforts to meet net-zero emissions targets. In 2023, flaring alone contributed approximately 381 million tonnes of CO_2 equivalent emissions, representing up to 9% of the oil and gas industry's scope 1 and 2 emissions [1, 2]. The need for decarbonizing this sector has become increasingly urgent as emissions from flaring and venting remain significant. The International Energy Agency (IEA) has set ambitious targets, calling for the elimination of all non-emergency flaring by 2030 to achieve net-zero emissions by 2050. Currently, under the EU Emissions Trading Scheme (ETS), a < 7.5 % uncertainty level is required for flare gas measurement, highlighting the challenges inherent in achieving precise measurements for such flows. Although progress has been limited to date, it is anticipated that strengthened policies and industry initiatives will support this goal.

Flaring and venting allow for the controlled release of excess gases that cannot be processed safely, preventing risks to both personnel and infrastructure. Flare and vent gases primarily consist of methane and other hydrocarbons, which are either vented directly or flared by converting the methane to CO_2 through combustion. Since methane has a shorter atmospheric lifetime but a much higher global warming potential than CO_2, controlled flaring can, paradoxically, reduce the overall environmental impact of hydrocarbon production by converting methane emissions into CO_2.

Accurate metering of flare and vent gases is crucial for several reasons. Beyond regulatory compliance, reliable measurement ensures that flare systems are purged adequately, reducing the risk of forming combustible gas mixtures that could lead to flashbacks or burn-backs within the flare stack. Errors in metering can lead to sub-optimal flare system operation, potentially increasing greenhouse gas emissions. Consequently, flaring and venting systems must be operated above their minimum safety flow rates and, in the case of flaring, achieve high combustion and destruction efficiencies to minimize emissions.

Computational Fluid Dynamics (CFD) is widely used to correct ultrasonic meters (USMs), which are the most common meters in flare gas applications, for installation effects. However, this

approach raises two critical questions: is the CFD model properly validated, and what is the uncertainty associated with the CFD-derived k-factors? Quantifying this uncertainty is essential for calculating the overall uncertainty budgets in flare gas measurement [3]. This paper aims to address these questions.

This work follows the ASME V&V 20-2009 Standard for Verification and Validation in Computational Fluid Dynamics and Heat Transfer [4], which offers a framework for assessing the accuracy of computational simulations through comparison with test data. By determining both the model error and associated uncertainty, this approach supports the development of a comprehensive uncertainty budget for flare gas flows, ultimately contributing to more reliable measurement practices that align with industry sustainability goals.

2 EXPERIMENTAL TESTS AT NATIONAL ENGINEERING LABORATORY

To produce suitable experimental data, necessary for the validation exercise, tests were carried out at the high-pressure dry gas facility of TÜV SÜD National Engineering Laboratory (NEL). A CAD image of the facility is shown in Figure 1. The device under test (DUT) was a single-path diametric ultrasonic meter which was used across seven different installations: a baseline test with over 55 diameters of straight upstream pipe, followed by installations at 5, 10 and 20 diameters downstream of a single in-plane bend; and 5, 10 and 20 diameters downstream of an out-of-plane bend. The installations are shown in Figures 2-4, while images of the test sections installed in the facility are included in the Appendix.

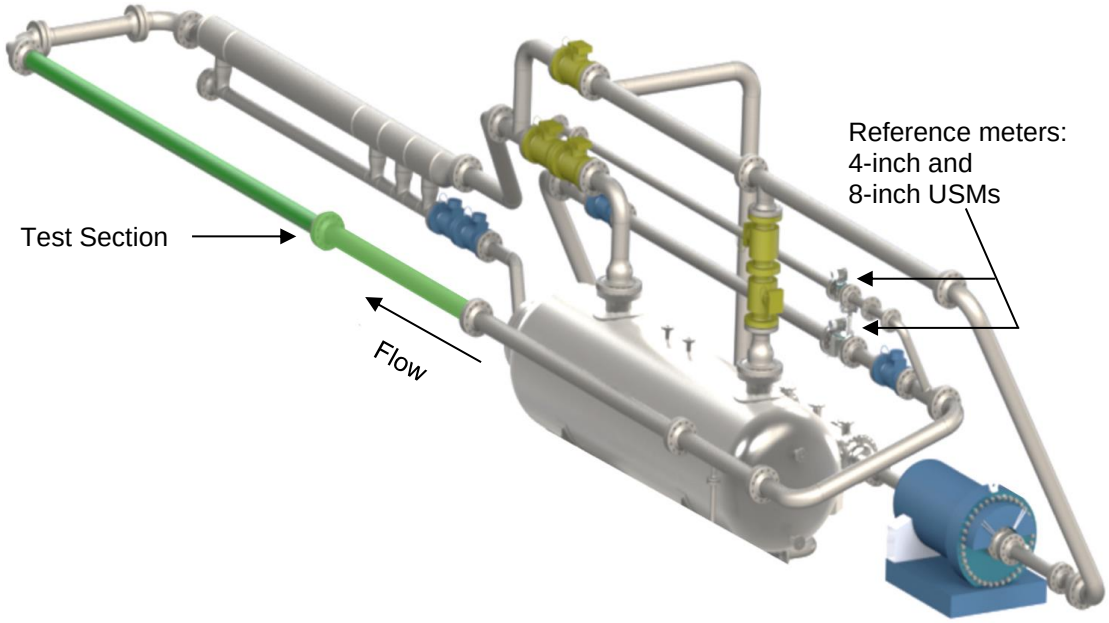

Figure 1 – CAD image of the high-pressure dry gas facility of NEL with the test section and the reference meter locations labelled

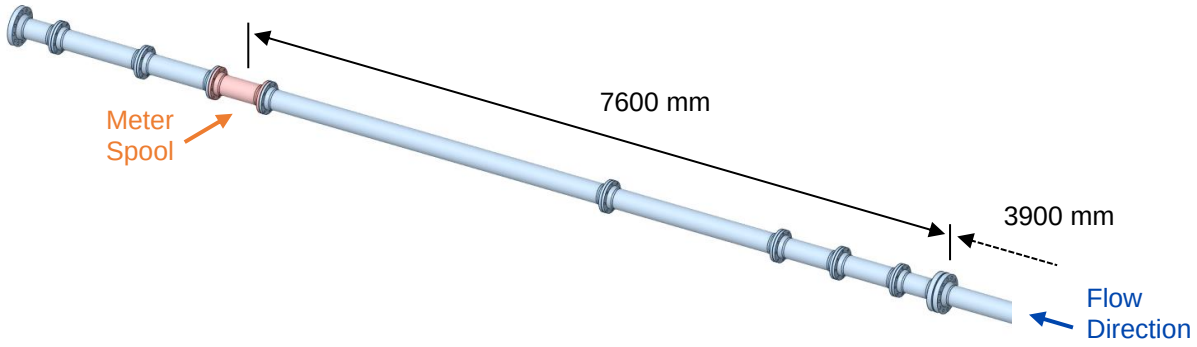

Figure 2 – Straight “Test A” Section

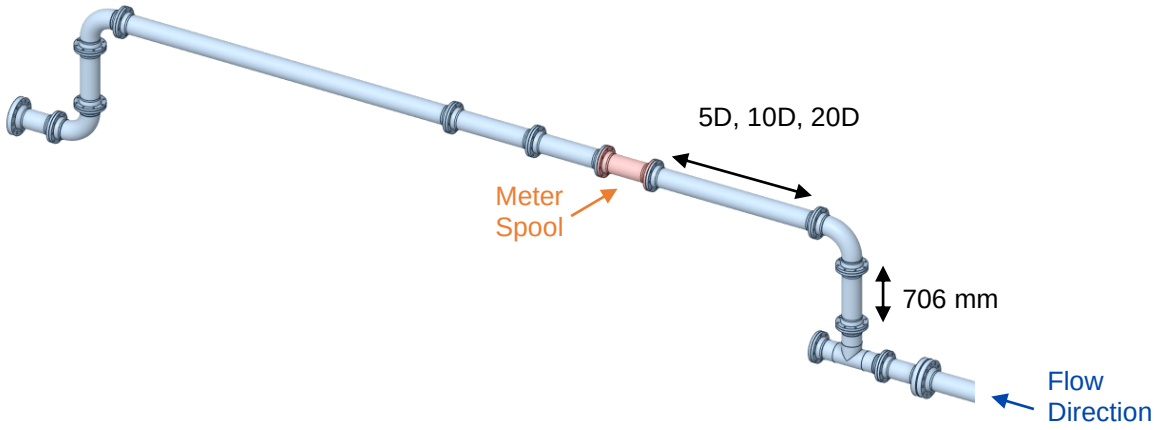

Figure 3 – In-plane bend “Test B” Section

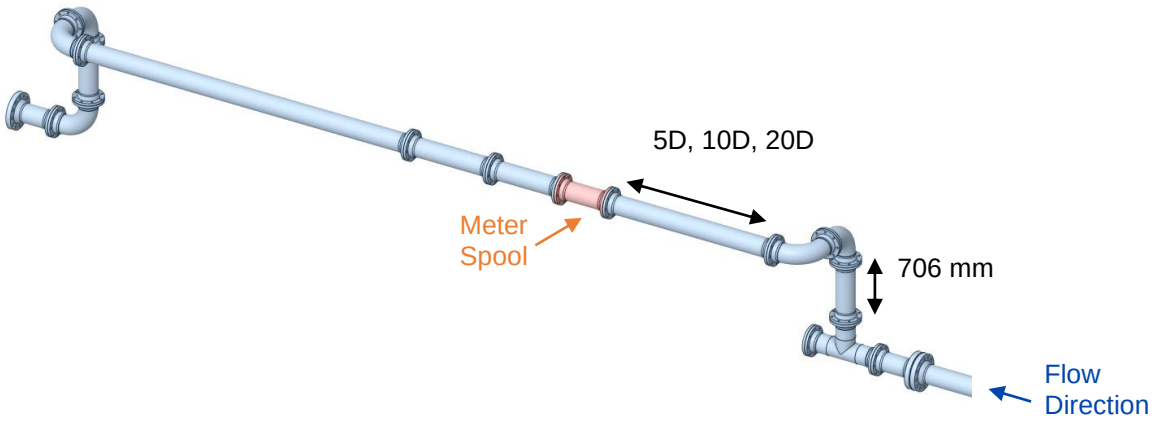

Figure 4 – Out-of-plane bend “Test C” Section

Nitrogen was used for the tests at nominal pressures of approximately 1 barg and 10 barg, with a nominal temperature of 20 °C, and flow rates ranging from 30 m³/h to 2270 m³/h. This equates to flow velocities from 0.25 m/s to approximately 20 m/s and Reynolds numbers in the range of

6,000 to 3,000,000. At each test point, 3 to 6 readings were taken, each over a period of 180 seconds. In total, 189 test points were measured to comprehensively capture the range of conditions across all seven installations.

The gas reference volumetric flow rate was measured using one of two calibrated and fully traceable SICK FLOWSIC600-XT, 4-path USMs; these meters cover a nominal flow rate range of 20 m^3/h to 2500 m^3/h. In these tests, the 8-inch meter was used for nominal flow rates over 100 m^3/h and the 4-inch meter for flow rates at or under this value. All static pressure, differential pressure, and temperature measurements were taken using traceable calibrated instrumentation. The device under test was a single-path, 8-inch, diametric ultrasonic meter provided by SICK.

The effect of three installation conditions (Test A, Test B and Test C) were investigated. Results from the baseline (Test A) and in-plane bend (Test B) configurations show consistent over-reading across all Reynolds numbers, with errors increasing at Reynolds numbers below 200,000. In contrast, tests with out-of-plane bends (Test C) reveal differing trends in meter error with Reynolds number as the meter position changes.

A single bend creates an asymmetric flow profile with non-axial velocity components. The curvature of the bend forces the flow towards the wall of the pipe, resulting in a skewed velocity profile that gradually develops further downstream. This effect is even more pronounced with out-of-plane bends, where the induced swirl has a lasting impact on flow behaviour.

Typically, manufacturers may recommend 20D of straight upstream pipe to mitigate installation effects; however, these results, illustrated in Figure 5, demonstrate that this length may be insufficient after out-of-plane bends that generate swirl. Although the effect of an in-plane bend is relatively small, a 6 % difference can be seen between the straight test results and the results where the meter is placed at 20D downstream of the out-of-plane bend.

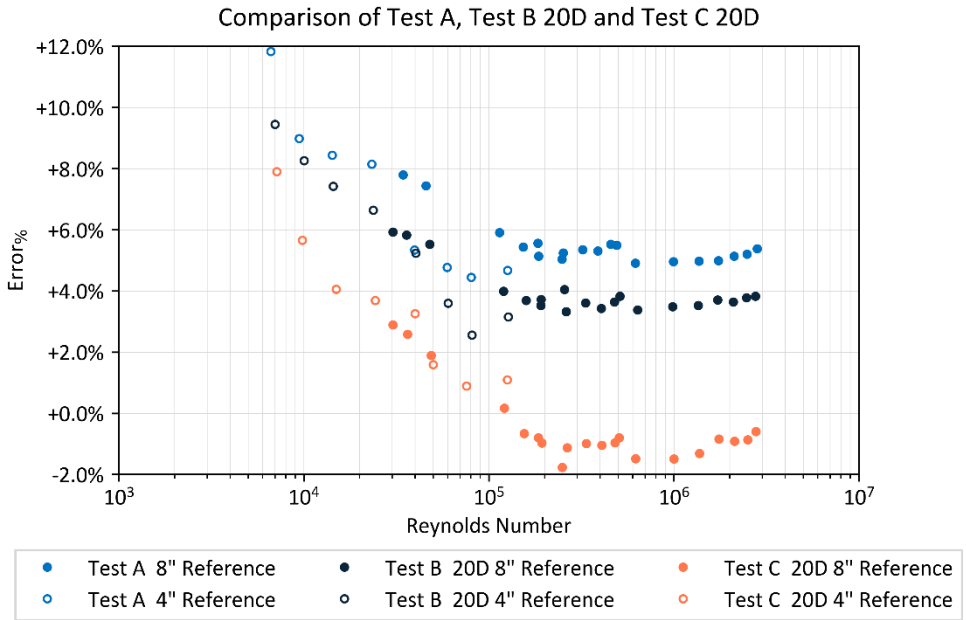

Figure 5 – Comparison of test results from the straight section (Test A), and 20D downstream from the in-plane (Test B) and out-of-plane (Test C) bends

Overall, the experimental data obtained at TÜV SÜD National Engineering Laboratory enable a thorough validation process, with the validation experiments supplying the simulation inputs along with their associated uncertainties. Collaboration between modelers and experimentalists was essential in designing these validation experiments to ensure that all relevant information

was effectively integrated. This joint approach is critical for achieving an accurate and meaningful validation, as it allows the simulation model to be benchmarked against rigorously designed experimental conditions.

3 CFD VALIDATION PROCEDURE

In the validation process a simulation result, S, is compared with an experimental result, D, for specified validation variables at a specified set of conditions (validation point). A schematic for our case is given in Figure 6, where S is the k-factor derived from the CFD simulation, k_S, and D is the k-factor from the experiment, k_D.

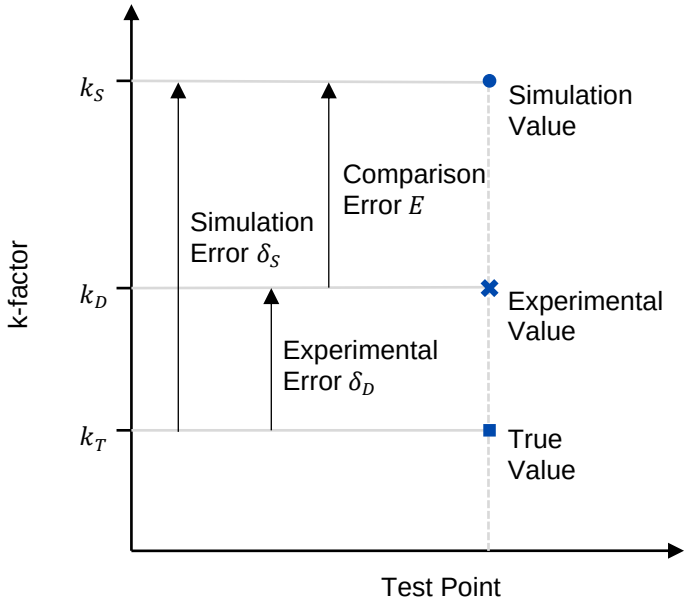

Figure 6 – Comparison of experimental and simulation data at a test point illustrating the different errors

All errors in the simulation result, δ_S, can be assigned to either the error due to modelling assumptions, δ_{model}, the error due to the numerical solution of the equations, δ_{num}, or the error due to the simulation input parameters, δ_{input}. This read

$$\boldsymbol{\delta_S = \delta_{model} + \delta_{num} + \delta_{input}}. \quad (1)$$

The comparison error can be therefore written as

$$\boldsymbol{E = k_S - k_D = \delta_S - \delta_D = \delta_{model} + \delta_{num} + \delta_{input} - \delta_D}, \quad (2)$$

rearranging this gives

$$\boldsymbol{\delta_{model} = E - (\delta_{num} + \delta_{input} - \delta_D)}. \quad (3)$$

The objective of the validation exercise is to estimate δ_{model} within an uncertainty range. The comparison error can be easily determined, however, the remaining errors of Equation 3 are unknown. The standard uncertainties corresponding to these errors are u_{num}, u_{input}, and u_D. The validation standard uncertainty, u_{val}, is defined as the estimate of the standard deviation of the parent population of the combination of errors $(\delta_{num} + \delta_{input} - \delta_D)$ and consequently

$$\boldsymbol{\delta_{model} \in E \pm u_{val}}. \quad (4)$$

If all three errors are effectively independent then

$$\boldsymbol{u_{val} = \sqrt{u_{num}^2 + u_{input}^2 + u_D^2}}. \quad (5)$$

However, this does not apply if the experimental and computationally predicted values are functions of shared variables. In that case δ_{input} and δ_D are not independent and therefore the equation used is

$$\boldsymbol{u_{val} = \sqrt{u_{num}^2 + u_{input+D}^2}}. \quad (6)$$

To summarise, E, is an estimate of δ_{model} and the validation standard uncertainty, u_{val}, is the standard uncertainty of that estimate. Both E and u_{val} are the validation metrics [4].

The sections that follow outline the approach used in this work to evaluate the numerical uncertainty through grid convergence, estimate the model error, and the finally calculate the validation uncertainty. It should be noted that the following validation procedure is specifically tailored to the problem addressed in this study; for other types of problems, readers are encouraged to consult the standard guidelines [4].

3.1 Numerical Uncertainty

To quantify the numerical uncertainty of the solution, the Grid Convergence Index (GCI) method was used [4, 5, 6]. This step is also referred to as solution verification.

According to this method, a mesh independence study must be conducted using at least three meshes with progressively smaller representative cell sizes, denoted as cell sizes h_3, h_2 and h_1. For unstructured grids, like those in this study, the representative cell size is defined as

$$\boldsymbol{h = \left(\frac{\sum_{i=1}^{N} \Delta V_i}{N}\right)^{\frac{1}{3}}}, \quad (7)$$

where N is the total number of cells of the mesh and ΔV_i is represents the volume of each cell. The grid refinement factor, $r_{21} = h_2/h_1$, is generally recommended to be greater than 1.3 for most practical applications [4]. However, other publications [5,6] which also examine spatial convergence using this method, suggest that ratios only need to exceed 1.1 to distinguish numerical error from other sources like convergence error and computer round-off. The apparent order of convergence, p, is then calculated using the method discussed in [4,5,6].

The fine Grid Convergence Index is then calculated as:

$$\boldsymbol{GCI_{fine} = \frac{F_s\, e_a^{21}}{r_{21}^{\,p} - 1}}, \quad (8)$$

using the absolute approximate error between the solution on the two finest meshes, $\boldsymbol{e_a^{21}}$, and the factor of safety $\boldsymbol{F_s}$. In this work, $\boldsymbol{F_s = 3}$ was considered since it provides a more conservative value of numerical uncertainty and is recommended to obtain a GCI for unstructured grid refinement [4]. The absolute GCI corresponds to the absolute expanded numerical uncertainty, $\boldsymbol{U_{num}}$, at 95 % confidence.

When a design or analysis activity involves numerous CFD simulations (e.g., a DOE study), it may be practical to use the medium grid h_2. In such cases, it becomes important to quantify the

error associated with the medium grid. The GCI for the medium grid, GCI_{medium}, is calculated by multiplying GCI_{fine} by a factor of ${r_{21}}^{p}$.

The standard numerical uncertainty is then calculated by dividing the GCI by a coverage factor of $F = 1.15$, as the error distribution around the fine grid solution is approximately a shifted Gaussian [4]. The conservative value of u_{num} is then obtained as:

$$\boldsymbol{u_{num} = \frac{U_{num}}{F} = \frac{GCI}{1.15}}. \quad (9)$$

An example of the GCI method is presented in Table 1 where both GCI_{fine} and GCI_{medium} are calculated. Considering the simulation objectives, a nominal simulation case representative of the problem to be studied, is defined. A detailed mesh independence study is performed for the nominal case as stated above. Based on the results of this study a base mesh resolution that achieves the simulation objectives at the estimated accuracy is selected. This base mesh resolution is then used for all subsequent simulations run for this particular problem. The numerical uncertainty calculated for the nominal case is assumed to remain the same for all subsequent simulations.

Table 1 – Example of the GCI method used to calculate numerical uncertainty

Resolution	Total number of cells N	Total volume of mesh V (mm^3)	h	r	k-factor	p	e_a	GCI	u_{num}
Fine	1.20E+07	4.69E+08	3.39	1.31	0.94872	1.98	4.00E-05	1.67E-04	0.015345 %
Medium	5.32E+06	4.68E+08	4.45	1.32	0.94868	-	7.00E-05	2.90E-04	0.026558 %
Coarse	2.32E+06	4.68E+08	5.86	-	0.94861	-	-	-	-

3.2 Input and Experimental Uncertainty

An additional source of uncertainty in CFD simulations arises from uncertainties in the input parameters, denoted as u_{input}. Each input, including fluid properties and boundary conditions, introduces corresponding uncertainty into the simulation output. Given that the solution depends on multiple parameters (such as density, viscosity, and volumetric flow rate), the influence of each parameter must be considered.

There are two methods for quantifying this uncertainty: the Sensitivity Coefficient (Local) method and the Sampling (Global) method [4]. The Sensitivity Coefficient method calculates sensitivity coefficients for each input variable, which are then combined to estimate the model input uncertainty. This approach is considered local because function evaluations (simulations with a single parameter vector value) occur within a narrow range around the mean parameter vector value, making it unable to account for highly nonlinear behaviours across the parameter space. To address this limitation, a global method is employed in this study.

The Monte Carlo method, a reliable global sampling technique for uncertainty analysis, uses numerous random samples from the input parameters probability distribution functions to generate statistical properties of the model output. However, it may require tens of thousands of function evaluations to achieve statistical convergence (where results no longer depend on the number of function evaluations).

An alternative, less computationally intensive approach is Latin Hypercube Sampling (LHS), which is applied in this study. In LHS, each input variable's cumulative distribution function is

divided into n_{LHS} bands of equal probability. One random sample is drawn from each band, resulting in n_{LHS} samples, and this process is repeated for all model parameters. Although LHS demands fewer resources than the Monte Carlo method, approximately 4000 simulations were still necessary in this work, which remains computationally intensive.

The validation variable in this study is the k-factor of the USM calculated as

$$\boldsymbol{k_D = \frac{V_{Ref}}{V_{USM}}}, \tag{10}$$

where V_{USM} is the measured USM velocity in the streamwise direction and V_{Ref} is the reference meter velocity at the location of the USM. The latter is calculated from the reference flow rate, $\dot{Q}_{Ref}$, and the pipe area at the location of the meter under test, A, using $V_{Ref} = \dot{Q}_{Ref}/A$. The validation variable resulting from the simulation, k_S, reads

$$\boldsymbol{k_S = \frac{V_{Ref}}{V_{CFD}}}, \tag{11}$$

where V_{CFD} is the equivalent of V_{USM} as computed from the numerical simulation. To replicate the tests, the input parameters required for the simulations were the density, ρ, and viscosity, μ, at the meter under test, and the reference flow rate $\dot{Q}_{Ref}$ measured.

Based on the above, the validation variable is determined using a data reduction equation that combines experimentally measured variables. Additionally, some measured variables share common sources of error. For instance, both density and viscosity calculations rely on measured temperatures. On top of this, k_D and k_s share a dependence on the same measured variable, $\dot{Q}_{Ref}$. Consequently, there is no explicit expression for u_{input} as its components combine implicitly with components of u_D. Therefore, we calculate $u_{input+D}$ instead. While V_{USM} is not a direct input for simulation, it is treated here as both input and experimental parameter. To summarise, the input parameters considered in this study are density, viscosity, (both at the location of the USM under test) reference flowrate and velocity from the USM.

The sampling methods require assumptions regarding the probability distribution of the input parameters. In this study, these parameters are assumed to follow a normal distribution, with standard uncertainty, u, representing the standard deviation of this distribution. The nominal value from the experiment is used as the distribution mean.

The standard uncertainties, $u_{parameter}$, and the nominal values of the input parameters were used to generate 10 random samples per input parameter using the Latin Hypercube Sampling (LHS) method. The selected number of samples limits the computational cost and at the same time is adequate for this application. To test this, the sampling was repeated for a test point with the random number generator set to different seeds, yielding consistent results, which confirmed that 10 samples were sufficient. The standard uncertainties and two example Latin Hypercube samples, out of 10 for a single test point, are shown in Table 2.

These random samples are used to perform 10 distinct simulations for a single test point. For each set of random samples, i, the experimental result, D_i, (using Equation 10 here) and the simulation result, S_i, (Equation 11) are calculated.

It may seem counterintuitive, but the experimental results used to determine the comparison error, and the input parameter uncertainty are not those recorded directly during the tests. Instead, these values are recalculated for each sample to reflect the range of possible k-factor values that could have been measured at a specific test point.

An example of this process for a single test point is shown in Table 3. For each sample, the comparison error, i.e. the difference between the CFD-derived k-factor, k_S, and the experimental one, k_D, was calculated as $E = k_S - k_D$.

Standard statistical methods are applied to these values to calculate the uncertainty from the LHS samples. At the bottom of each column, the mean and standard deviation are provided. The means represent the nominal (expected) values for the simulated (k_S) and experimental (k_D) k-factors and their difference (E). The estimated standard deviations in each column represent the standard uncertainties due to input parameter uncertainty (u_{input}), the experimental uncertainty due to measurement uncertainty (u_D), and the combined contribution of these uncertainties to the validation uncertainty ($u_{input+D}$).

Table 2 – Parameter standard uncertainties and example Latin Hypercube samples

Parameter	Impact	Nominal Value	Standard Uncertainty	Latin Hypercube Sample 1	Latin Hypercube Sample 2
Density (kg/m^3)	k_S	12.6188	0.1653	12.5687	12.6360
Viscosity (Pa s)	k_S	1.7736E-05	9.0641e-08	1.7709E-05	1.7746E-05
Reference Volumetric Flowrate (m^3/s)	k_D and k_S	0.6326	1.1444e-03	0.6323	0.6327
USM Velocity (m/s)	k_D	20.6551	0.0580	20.6375	20.6612

Table 3 – Indicative results of the sampling method for a single test point

Sample Number	k_S	k_D	E
1	0.9706	0.9492	0.0213
2	0.9706	0.9488	0.0217
3	0.9706	0.9482	0.0223
4	0.9706	0.9491	0.0215
5	0.9706	0.9479	0.0226
6	0.9706	0.9485	0.0221
7	0.9706	0.9465	0.0241
8	0.9705	0.9497	0.0209
9	0.9705	0.9498	0.0208
10	0.9705	0.9508	0.0197
Mean	0.9706	0.9489	0.0217
Standard Deviation	2.53E-05	1.11E-03	1.14E-03

3.3 Validation Uncertainty

After calculating the numerical uncertainty, u_{num}, following the procedure outlined in Section 3.1 and determining the combined input and experimental uncertainty, $u_{input+D}$, as described in Section 3.2, the validation uncertainty, u_{val}, can be calculated using Equation 6.

It should be noted that the solver used has many adjustable parameters, such as numerical schemes and turbulence models, that are herein considered fixed and are thus part of δ_{model}. The simulation inputs which have uncertainties that are accounted for in this work, i.e., ρ, μ, and $\dot{Q}_{Ref}$, do not contribute to δ_{model} but to δ_{input}.

4 METHODOLOGY

4.1 Geometry

CFD simulations were carried out to replicate the experiments conducted at NEL and to compute the CFD-derived correction factors for a single path diametric meter.

Two modelling approaches were considered. One with the transducer geometry explicitly modelled and one without. For the baseline test (Test A) the USM was placed having over 55D of straight upstream pipe. For the in-plane bend test section (Test B), the USM was placed at 5, 10 and 20D downstream of the single in-plane bend. Finally, for the out-of-plane bend test section (Test C) the meter was placed at 5, 10 and 20D downstream of an out-of-plane bend.

For each of the above 7 different installations, one CFD model is generated including the transducers geometry. For the CFD models where the transducers geometry is not explicitly accounted for, only 3 models need to be generated, one for each piping configuration. This resulted in the use of 10 distinct geometries.

Figure 7 shows indicative fluid volumes used in the CFD modelling. The model begins at the straight section after the inclined bend from the reference meters and extends to the end of the 8-inch straight section.

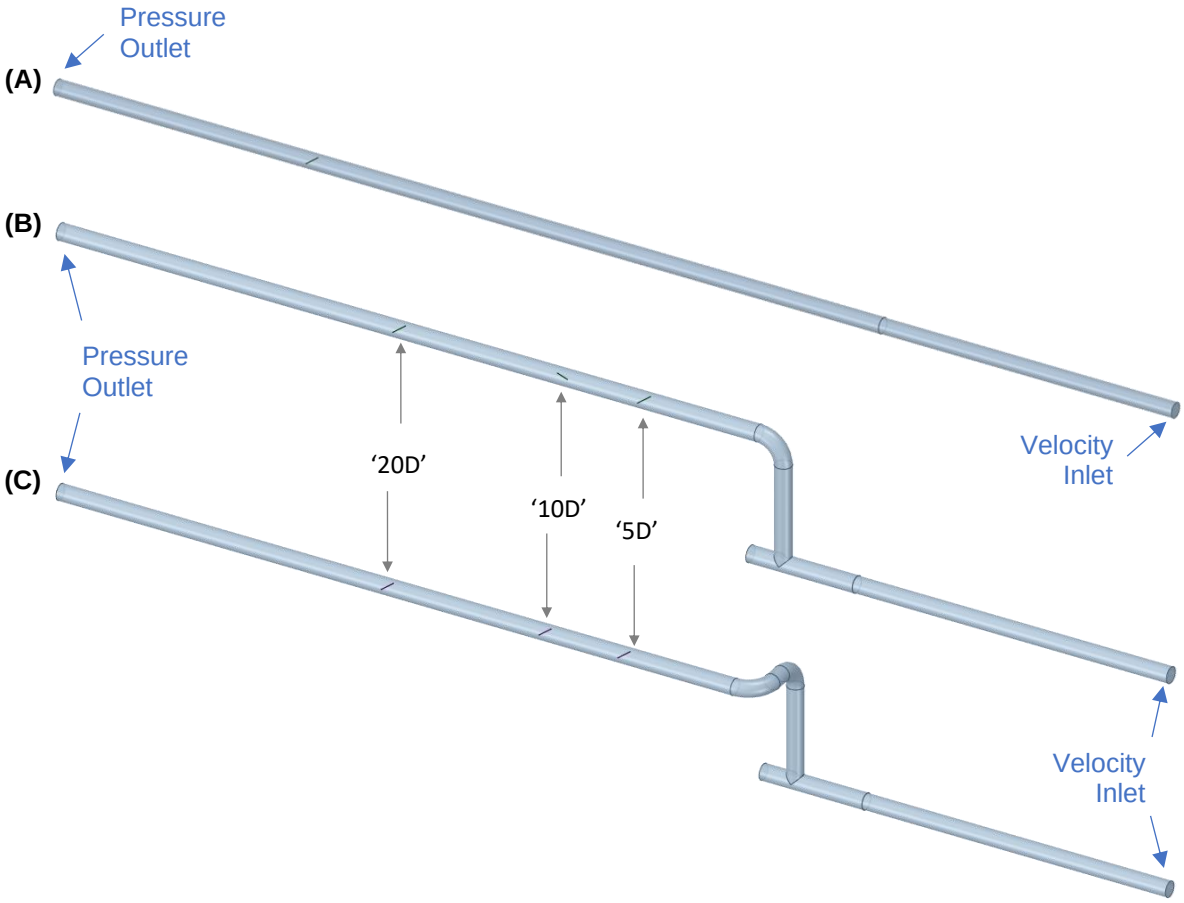

Figure 7 – Fluid volumes of (A) Test A without the transducers (B) Test B without the transducers, showing locations of the 5D, 10D and 20D meter paths, and (C) Test C without the transducers, showing locations of the 5D, 10D and 20D meter paths

4.2 Mesh

The governing partial differential equations of fluid dynamics are non-linear, and therefore require numerical solution. To enable this, the fluid domain must be divided into smaller subdomains (cells). The equations are discretised and solved iteratively within each cell. For all geometries in this study, a polyhedral mesh was employed to discretise the domain.

Each mesh included refined prism cells near the walls to capture the high velocity gradients in these regions and fully resolve the flow at the boundary layer. A first cell height of 0.009 mm was chosen to achieve a dimensionless wall distance, y^+, of approximately 5 for the highest Reynolds number. This same mesh was used at lower Reynolds numbers, resulting in $y^+ < 5$.

To estimate numerical uncertainty, mesh independence studies were conducted following the method discussed in Section 3.1. Separate studies were performed for each of the three tests (Tests A, B, and C) with and without transducers, totalling 6 grid studies. For Tests B and C, the study focused on the 5D position of the meter, where the flow is expected to be most challenging. For each configuration, numerical uncertainty was calculated for the test point with the highest flowrate (also the highest Reynolds number in this work). This value of u_{num} was then considered constant for all the test points of the same piping installation.

The reason we follow this approach is explained by the ASME V&V standard [4] which suggests that the grid convergence study should be performed for a nominal case. From the solution verification results of this nominal case, a base grid resolution is established that meets the

simulation accuracy objectives. This base grid resolution is then applied in all subsequent simulations for the specific problem.

In each grid study, three meshes were created based on the parameters outlined in Table 4. For geometries without transducers, the minimum cell size was 1 mm; for those with transducers, it was reduced to 0.2 mm to capture finer features. Throughout the study, the total prism layer height was kept constant, with successive refinements applied to both bulk fluid and prism layer cells to maintain consistent wall-adjacent cell height and a proportional size ratio between the outer prism layer and bulk polyhedral cells. This setup provided a grid refinement factor of approximately 1.3 $(1.25 \leq r \leq 1.35)$, meeting the requirements of the GCI method.

Table 4 – Mesh size settings used in grid study

Resolution	Max Cell Size (mm)	Number of Inflation Layers	Wall-Adjacent Cell Height (mm)	Prism: Polyhedral Cell Size Ratio	Inflation Layer Height (mm)
Coarse	10	15	0.009	0.5	13.7 (approx.)
Medium	7.5	20			
Fine	5.65	26			

As a result of the six mesh independence studies, the fine resolution was selected for the remainder of this work, with corresponding numerical uncertainties u_{num} calculated and later applied in the calculation of u_{val} using Equation 6. Table 1 illustrates that u_{num} for the fine mesh is low. While using the medium mesh and its larger uncertainty from the GCI analysis would also have been acceptable, the fine mesh was preferred for its manageable computational size and enhanced accuracy.

Figure 8 shows the polyhedral mesh at the inlet, while Figure 9 displays it at the meter location and transducer heads. For each geometry, the fine mesh resolution included approximately 12 to 15 million cells.

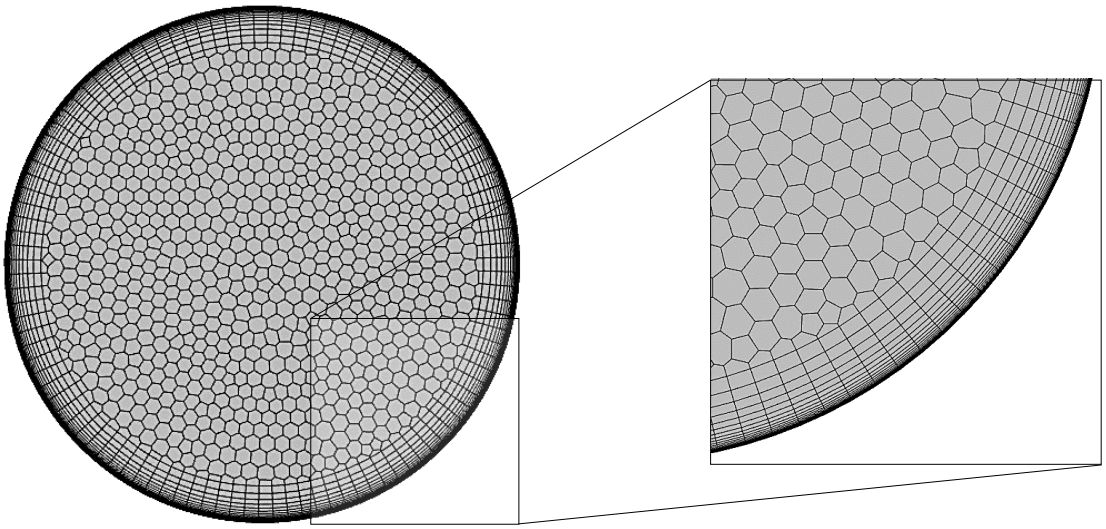

Figure 8 – Mesh at the inlet of the domain (fine resolution) with an exploded view of the inflation layers

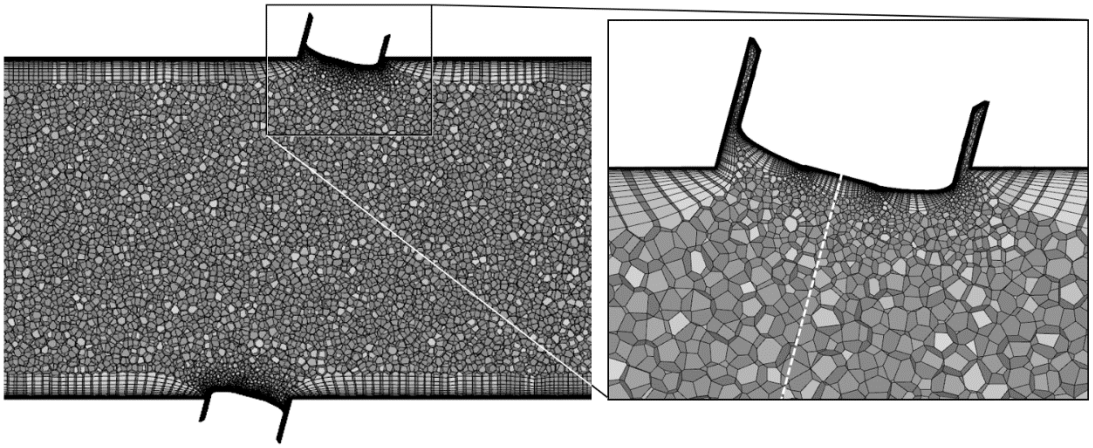

Figure 9 – Cross-section of the mesh (fine resolution) with transducers at the meter location with an exploded view of the mesh around the transducer head and dotted white line indicating the meter path

4.3 Modelling

Apart from the input parameters, all model settings were kept constant across all simulations, (as mentioned in Section 3.2) forming the simulation "model" with an associated error δ_{model}. All steady-state simulations were conducted using ANSYS Fluent 2021 R2. The realizable k-ε turbulence model with enhanced wall treatment was applied, and all discretization schemes were second-order accurate. Flows were assumed incompressible, with smooth walls, and the gravity effects were neglected.

While uncertainties in input parameters ρ, μ, and $\dot{Q}_{Ref}$, were considered, the geometry was assumed fixed. At the operating temperature of 20 °C, thermal expansion effects were negligible, allowing geometric changes to be ignored.

4.4 Simulations

Simulations were conducted for all points in the test matrix to replicate the experimental conditions, with each test comprising around 14 points at nominal gauge pressures of 1 bar and 10 bar. This covered Reynolds numbers ranging from approximately 6,000 to 3,000,000. Around 4,000 simulations were performed to calculate $\mathbf{E}$, $\boldsymbol{u}_{\boldsymbol{input+D}}$ and finally $\boldsymbol{u}_{\boldsymbol{val}}$ following the process discussed in Section 3.

4.5 Parameter and input uncertainties

Table 5 summarizes the sources of uncertainty used to estimate parameter uncertainty. Three error sources were considered: calibration uncertainty (from instrument calibration), repeatability (from the standard deviation of repeated readings), and scatter. For each reading, a standard deviation was observed in the USM measurements recorded during testing. The average of these values across all repeats for a given test point represents the scatter uncertainty. This scatter uncertainty was particularly notable for the USM's velocity readings in Tests B and C where unsteady effects were captured in each 180-second reading. This effect was more pronounced, where the meter was closer to the bends.

The uncertainties given in Table 5 are standard uncertainties. The standard uncertainty for each parameter, used in generating the LHS samples (see Section 3.2), is calculated as the square root of the sum of squares as follows:

$$\boldsymbol{u}_{\boldsymbol{parameter}} = \sqrt{\boldsymbol{u}_{\boldsymbol{calibration}}^{\boldsymbol{2}} + \boldsymbol{u}_{\boldsymbol{repeatability}}^{\boldsymbol{2}} + \boldsymbol{u}_{\boldsymbol{scatter}}^{\boldsymbol{2}}} \quad (12)$$

Table 5 – Input parameter uncertainties

Parameter	Uncertainty Source	Uncertainty Value
Density	Calibration	± 0.067 % (all flowrates)
	Repeatability	Standard deviation of repeat readings
Viscosity	Calibration	± 0.511% (all flowrates)
	Repeatability	Standard deviation of repeat readings
Reference Volumetric Flowrate	Calibration	± 0.180 % (> 120 m^3/h) ± 0.253 % (< 120 m^3/h)
	Repeatability	Standard deviation of repeat readings
	Scatter	Average of standard deviations of each repeat
USM Velocity (DUT)	Repeatability	Standard deviation of repeat readings
	Scatter	Average of standard deviations of each repeat

Ultrasonic flow meters generally show reduced accuracy at lower velocities. Specifically, across all tests, the standard uncertainty of the USM-measured velocity, u_{USM}, is higher at low reference meter velocities and decreases exponentially, reaching a stable level at higher velocities. For Test A, u_{USM} ranges from 0.25% to 1.6%. In Tests B and C, when the meter is installed 5D downstream of the last disturbance, u_{USM} ranges from approximately 0.8% to 4%, this uncertainty decreases to 0.6%–2.6% when the meter is positioned 10D or 20D downstream.

5 RESULTS

When comparing k_D with k_S across the two modelling approaches (with and without transducers), the model including transducers generally showed better agreement with experimental data in most of the 7 different setups. As a result, this modelling approach is recommended and as such, only these results are analysed in the following sections.

The validation uncertainties for the k-factor errors reported here are expanded (95% confidence). Therefore, the standard validation uncertainties calculated using Equation 9 are divided by the expansion factor $F = 1.96$ assuming a Gaussian error distribution.

In Test A, where a long straight section (55D) precedes the DUT, a fully developed flow profile is expected. According to the CFD model, this fully developed profile appears as early as 10D upstream of the meter, as shown in Figure 10. However, the 4-inch reference meter is located in a bypass section downstream of an out-of-plane bend, leading into the inclined test section (see Figure 1). Consequently, for test points using this reference meter, swirl effects might influence the flow in the test section. It's known that asymmetric velocity profiles can persist for over 50 pipe diameters downstream from their origin, while swirling velocity profiles can extend over 200 diameters downstream.

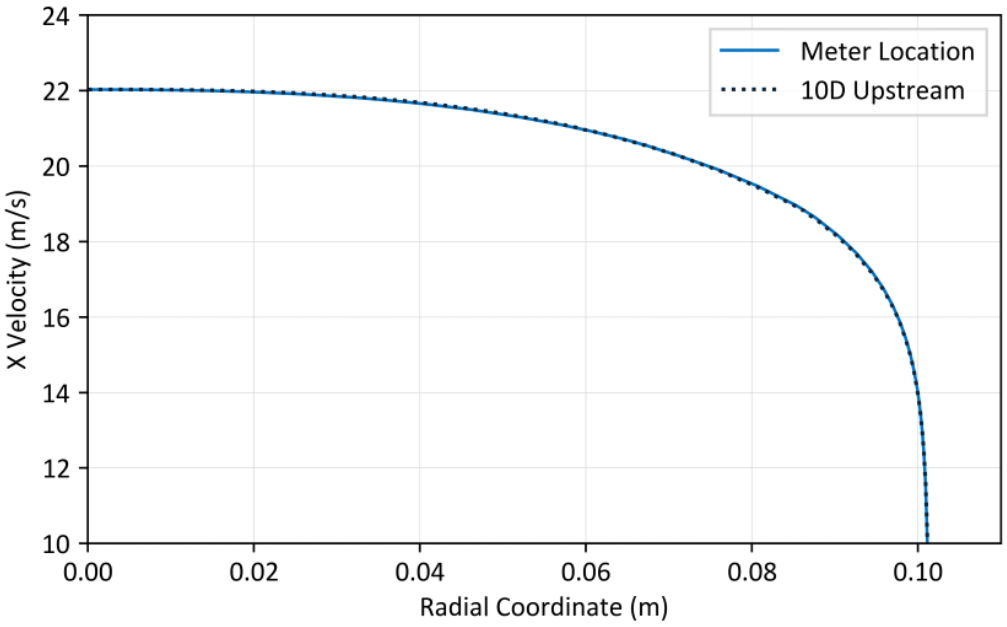

Figure 10 – Fully developed velocity profile at the meter location for the highest Reynolds test point of Test A

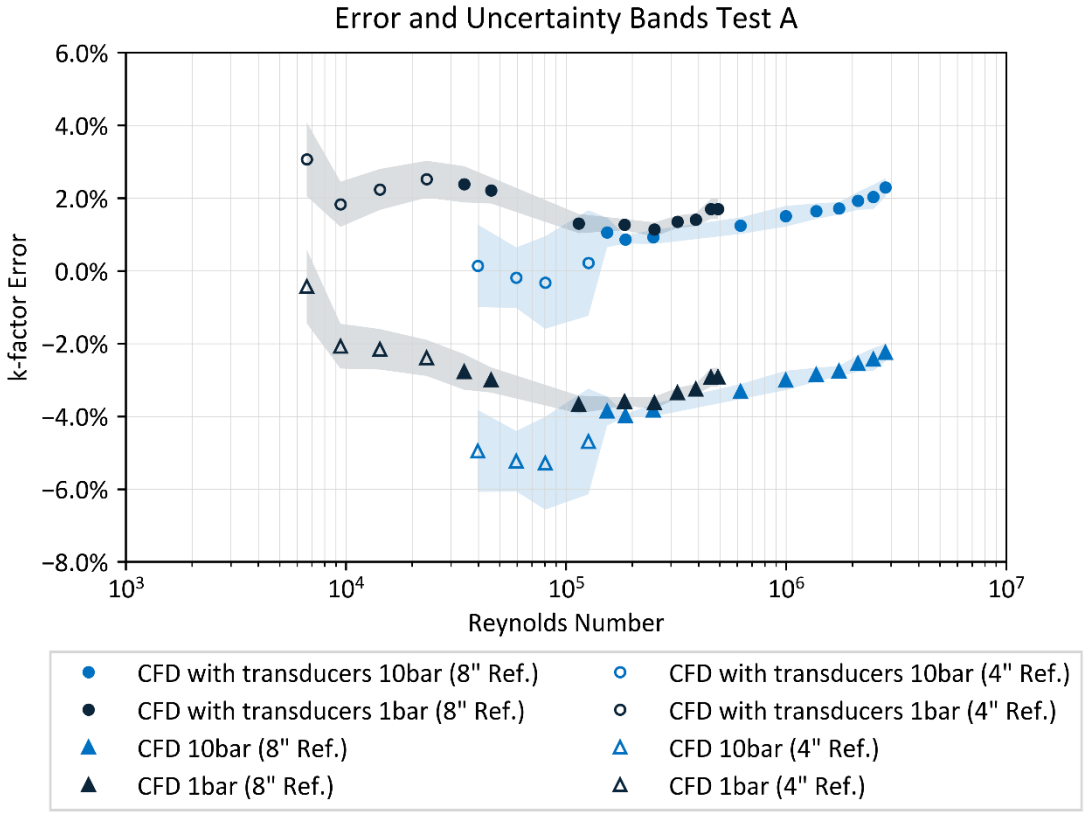

Figure 11 – Error and expanded uncertainty of the CFD-derived k-factor error for Test A. The results of both modelling approaches, including and excluding the transducers geometry, are displayed.

The results for Test A are shown in Figure 11. Outliers in these graphs may be due to the previously discussed flow effects. Specifically, the four lowest Reynolds number points in the 10-bar series, measured with the 4-inch reference meter, deviate from the trend observed in adjacent points.

Focusing on the results where the transducers are included in the model, the CFD-derived k-factor error ranges from -0.32% to 3.06%, with an uncertainty between 0.1% and 1.45%. Excluding the four apparent outliers, the maximum uncertainty for the CFD-derived k-factor error is 1.01%. Although no clear trend is evident in the CFD-derived k-factor error, its uncertainty remains below 0.4% for Re>150,000.

As outlined in Section 3.1, the same (small) u_{num} value was applied across all Test A points. The input parameter uncertainty u_{input} is negligible in this case. Therefore, the only factor affecting u_{val} as a function of Reynolds number is u_{USM} (which is related to u_D), as explained in Section 4.5.

At the time of writing this paper, the calculations for CFD k-factor errors and their associated uncertainties for Tests B and C are still in progress and are therefore not included here. However, the same methodology that was discussed in the previous sections applies.

6 IMPLEMENTATION OF RESULTS INTO UNCERTAINTY BUDGETS

6.1 Assessing the outcome of the validation process

The validation procedure confirms that the model predictions align with experimental observations within the assessed uncertainty range, providing an estimate of an interval within which δ_{model} falls with a given degree of confidence.

Based on the validation outcomes, there may be a desire to improve model accuracy or better understand the source of δ_{model}. If the original model is refined or modified to incorporate additional physics or different approaches (e.g., in turbulence modelling), it can be reassessed using the same procedure and experimental data.

Input parameters might also be reconsidered, as nominal values or uncertainty estimates may not fully apply to the validation experiment. Importance factors can reveal each parameter's contribution to the uncertainty in both the experimental data and simulation, indicating which parameters could affect δ_{model} significantly [4]. Evaluating improved models would require reducing the input parameter uncertainties through more carefully controlled or redesigned experiments.

For this study, possible model improvements include extending the model inlet further upstream to capture bends that might induce persistent swirl downstream of the reference meters, or testing alternative turbulence models. Additionally, for Tests A and B, test points measured at 10 bar using the 4-inch reference meter show relatively high experimental uncertainty, despite not being at low flow velocities where the meter typically underperforms. A possible solution is to rerun these test points using the larger 8-inch reference meter at 1 bar, as these points fall well within its range, potentially reducing the associated uncertainties. Alternatively, a flow straightener could be installed upstream of the DUT and (downstream of the inclined bend) to ensure flow disturbances from the bends do not persist through to the test section.

Despite these areas for potential improvement, the CFD-derived k-factor errors and their associated uncertainties for Test A are acceptable, allowing us to proceed confidently to the next phase of the analysis.

6.2 Implementation of the findings to derive CFD k-factor uncertainties

Having a satisfactory validation result, as in this study, we can explore how to apply these findings to actual flare gas lines. Typically, we model the flare gas line to compute the CFD-derived k-factors, but until now, we couldn't specify an associated uncertainty to incorporate into the overall uncertainty budget.

To proceed, certain assumptions are necessary, as the findings herein are based on a scaled-down, simplified configuration using a single-path diametric meter from a specific manufacturer. However, real flare gas lines are larger, sometimes up to 60 inches in diameter and 100 meters long, often with multiple bends, tees, and complex geometries leading to the flare gas meter. This meter could be single- or dual-path, configured as diametric or mid-radius.

For example, we considered an actual 14-inch flare gas line with a single-path diametric USM meter positioned 50D downstream of the last bend. CFD simulations were performed to compute the k-factors for 10 flow rates, covering the full operating range of the meter as requested by our customer. We then evaluated steps to estimate the uncertainty of these CFD-derived k-factors based on the findings of Test A.

First, we assumed that the relative comparison error, $E_{\%}$, of the CFD k-factors, k_{CFD}, as a function of Reynolds number from Test A could be applied to this flare gas line given certain similarities (upstream straight pipe length, meter configuration). Based on this, we can correct these k-factors as follows

$$\boldsymbol{k_{corrected} = 0.01\, k_{CFD}(100 - E_{\%})}. \quad (13)$$

Additionally, we assumed that the relative validation uncertainty, $u_{val\%}$, as a function of Reynolds number from Test A would also be applicable in this context.

Since the data available only corresponded to specific Reynolds numbers, we performed a curve fitting to interpolate between these values with minimal RMSE. We applied polynomial regression for both the relative comparison error, $E_{\%}$, and its corresponding relative validation uncertainty, $u_{val\%}$ (which represents the uncertainty in the error). To achieve a better fit, we divided the Reynolds number range into three sections for $E_{\%}$, applying a separate polynomial fit to each to ensure the smallest RMSE in each segment. We followed a similar approach for $u_{val\%}$, using two polynomial fits.

For the uncertainty budget, we considered the uncertainty of k_{CFD} to be equal to the numerical uncertainty u_{num} which was calculated following the procedure discussed in Section 3.1. In this case the expanded numerical uncertainty was 0.1 % for the whole range. The standard uncertainty from the curve fitting of $E_{\%}$ and $u_{val\%}$ was the corresponding RSME value ($u_{FIT_{E_{\%}}}$ and $u_{FIT_{u_{val\%}}}$ respectively).

For calculating Reynolds number uncertainty, we assumed the same density and viscosity uncertainties listed in Table 5, as no additional information was available for this specific installation. The repeatability of the USM velocity is indicated by the manufacturer as 0.5% (at 95% confidence). Finally, for the pipe diameter, an uncertainty of 1 mm (at 95% confidence) was assumed.

Using the aforementioned uncertainties, equations, and the uncertainty budget methodology described in GUM [7] the corrected CFD k-factors and their uncertainties were calculated. The

results are presented in Table 6 stating uncertainties at 95 % confidence. As indicated by $U_{FIT_{E_{\%}}}$ and $U_{FIT_{u_{val\%}}}$ the quality of the fitting of the $E_{\%}$ and $u_{val\%}$ curves improves with increasing Reynolds number. This is mainly due to the issue at intermediate Re, where the tests were conducted using the 4-inch reference meter at 10 bar operating pressure, as discussed in Section 5.

Excluding these specific points would create a clearer trend for $E_{\%}$ and facilitate polynomial fitting. The uncertainty ratio shown in Table 6 is the ratio between $U_{\boldsymbol{k_{corrected}}}$ and U_{val}. This ratio is quite large the first 4 lowest Reynolds numbers and decreases close to 1 for the rest.

This trend indicates that for higher Reynolds numbers, the validation uncertainty largely determines the uncertainty of the corrected CFD k-factors. At lower Reynolds numbers, however, the less precise fits for $E_{\%}$ and $u_{val\%}$ contribute significantly to the increased uncertainties of the corrected CFD k-factors.

Although we present figures of intermediate steps of the uncertainty implementation methodology in Table 6, the only two figures to be used in the USM meter to correct the flowrate is Re and $k_{corrected}$. The meters usually accept the k-factor information in a tabulated approach. The other figure necessary for the uncertainty budget is $U_{k_{corrected}}$ (%). A graph illustrating the original and corrected CFD k-factors with their associated uncertainties is presented in Figure 12.

Table 6 – Tabulated results

Re	k_{CFD}	$E_{\%}$	$k_{corrected}$	$U_{FIT_{E_{\%}}}$	$U_{val\%}$	$U_{FIT_{u_{val\%}}}$	$U_{\boldsymbol{k_{corrected}}}$ (%)	Unc Ratio
24,796	0.876	1.81	0.860	1.4201	0.52	0.1844	1.62	3.11
46,852	0.909	0.97	0.900	1.4201	0.27	0.1844	1.51	5.56
70,278	0.899	0.50	0.895	1.4201	0.13	0.1844	1.47	11.08
140,576	0.913	0.74	0.906	1.4201	0.28	0.1844	1.51	5.34
210,854	0.933	0.94	0.924	0.1432	0.86	0.1844	1.06	1.24
301,226	0.955	1.20	0.944	0.1432	1.32	0.1844	1.53	1.16
351,430	0.966	1.34	0.953	0.1432	1.06	0.1844	1.27	1.20
527,135	0.993	1.85	0.975	0.1432	0.21	0.0150	0.29	1.39
702,839	1.008	1.31	0.995	0.0893	0.34	0.0150	0.38	1.13
1,054,270	1.019	1.47	1.004	0.0893	0.58	0.0150	0.62	1.07

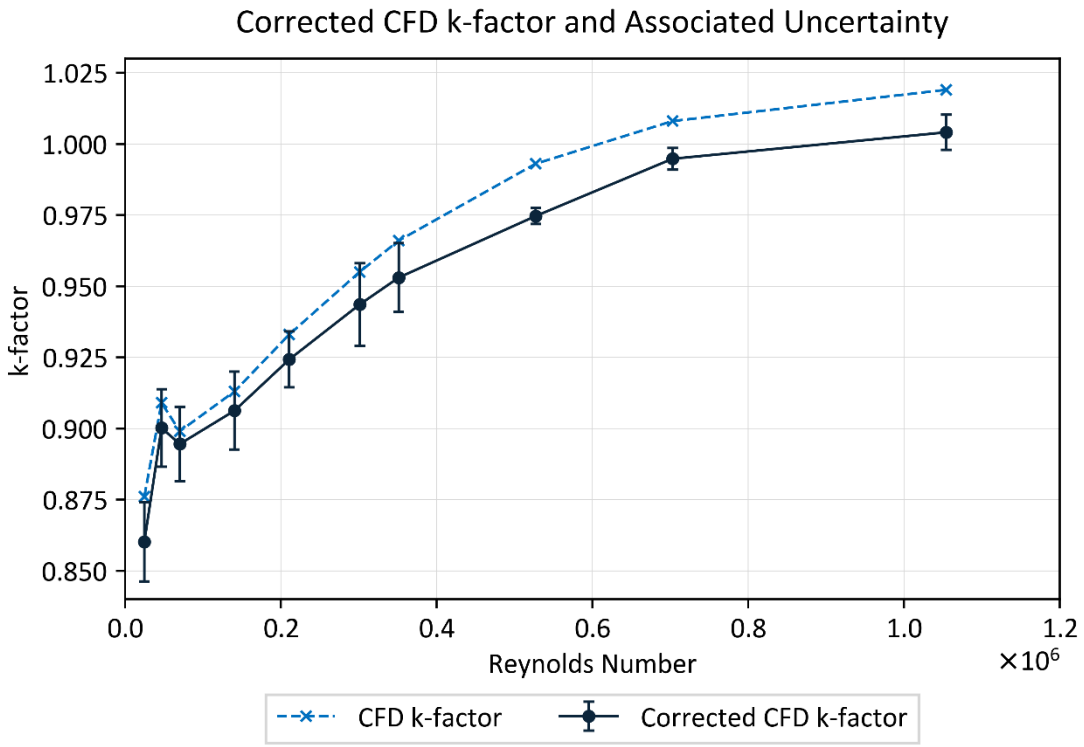

Figure 12 – The original CFD k-factors and the corrected ones for an actual flare gas installation. The corrected CFD k-factors and the associated uncertainties are derived using the findings of Test A.

7 CONCLUSIONS

Reducing emissions from flaring remains a critical aspect of global climate objectives, given that the practice still contributes substantially to the oil and gas industry's greenhouse gas emissions, including significant methane and CO_2 outputs. Regulatory bodies and initiatives, like the EU Emissions Trading Scheme and the IEA's call to eliminate non-emergency flaring by 2030, emphasize the need for precise measurement and control in flare gas systems to support environmental and safety standards. However, achieving the necessary measurement accuracy is complex due to flowrate variations and installation effects in flare gas systems. Computational Fluid Dynamics is widely used to correct ultrasonic flare gas meters to account for these effects. Despite its adoption, comprehensive validation of CFD models and calculation of associated uncertainties, essential for building complete uncertainty budgets, have not yet been undertaken.

To address this gap, we conducted multiple validation tests at NEL across various scaled-down flow configurations using a single path diametric ultrasonic flowmeter. Following the ASME V&V 20-2009 Standard, this work presented the methodology to validate CFD-derived k-factors, which involve calculations of the errors and uncertainties of those errors. We focused on the baseline results from straight pipe tests, while validation for other configurations is ongoing. Finally, we proposed a methodology to implement these findings in real flare gas systems, providing corrected CFD k-factors and their uncertainties.

Looking forward, we aim to complete the validation process for Test B and Test C results. Additionally, reducing the validation uncertainty by addressing key contributing factors—such as specific experimental or input parameter uncertainties—could be a valuable next step. This may involve rerunning simulations with a different modelling setup or repeating the experimental tests. Other methods for implementing these findings in uncertainty budget

calculations for real flare gas applications could also be explored, as the suggested approach here involved some assumptions.

Building on the foundational work presented in this study, further research to expand the experimental and CFD validation datasets will help cover a wider range of configurations, providing insights into additional realistic scaled-down scenarios. By testing different ultrasonic meter types, pipe sizes, and piping arrangements, we can better represent the diversity of actual flare gas system setups and address more possible installation effects. This expanded dataset would support our goal of developing flexible, applicable methods for calibrating CFD k-factors and calculating their uncertainty across various practical scenarios. Ultimately, this work could help establish robust, standardised guidance for achieving accurate flare gas measurements in diverse conditions, enhancing both regulatory compliance and environmental performance.

8 ACKNOWLEDGEMENTS

This work was funded by the UK Department for Science, Innovation and Technology (DSIT) through the National Measurement System Flow Programme.

The authors would like to thank SICK for providing the ultrasonic flowmeter used in the experiments described in this paper and for providing technical assistance during the testing program.

9 REFERENCES

[1] World Bank, “Global Gas Flaring Tracker Report,” World Bank Publications, 2023.

[2] IPIECA, IOGP and GGFR, “Flaring management guidance for the oil and gas industry,” London, IPIECA, 2022.

[3] American Petroleum Institute, “API Manual of Petroleum Measurement Standards (MPMS) 14.10 2nd edition, Natural Gas Fluids Measurement - Measurement of Flow to Flares,” 2021.

[4] The American Society of Mechanical Engineers, “ASME V&V 20-2009, Standard for Verification and Validation in Computational Fluid Dynamics and Heat Transfer,” ASME, 2009.

[5] P. J. Roache, “Perspective: A Method for Uniform Reporting of Grid Refinement Studies,” J. Fluids Eng, vol. 116, pp. 405-413, 1994.

[6] J. W. Slater, “Examining Spatial (Grid) Convergence,” NASA, Washington, 2021.

[7] BIPM, IEC, IFCC, ILAC, ISO, IUPAC, IUPAP, OIML, “Evaluation of measurement data - Guide to the expression of uncertainty in measurement,” Joint Committee for Guides in Metrology, JCGM 101:2008, 2008.

APPENDIX

Figure A1 – Image of straight (Test A) section facing upstream

Figure A2 – Image of in-plane bend (Test B) section with meter placed in the 20D position

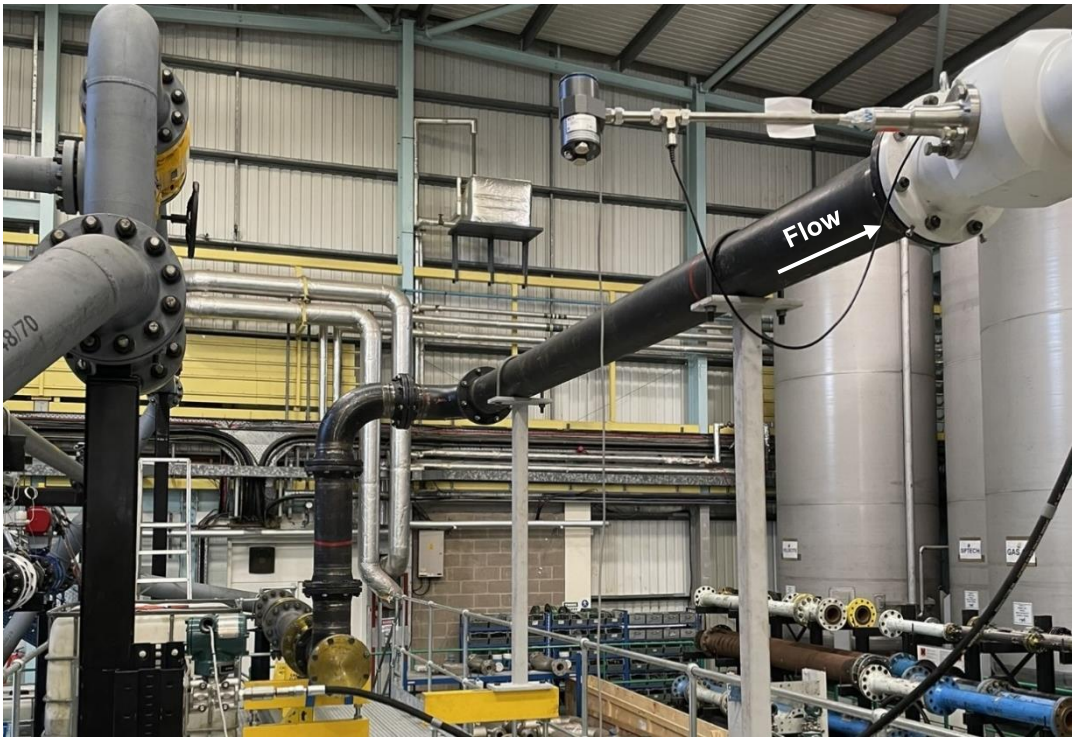

Figure A3 – Image of out-of-plane bend (Test C) section with meter placed in the 20D position